RSC Advances

PAPER

View Article Online
View Journal | View Issue

Cite this: *RSC Adv.*, 2022, **12**, 9660

Steered polymorphic nanodomains in TiO_2 to boost visible-light photocatalytic oxidation†

Zeju Zhang,‡[a] Mang Niu,‡[a] Wei Li,[a] Chenfeng Ding,*[be] Peitao Xie,[a] Yongxin Li,[a] Lili Chen,[a] Xiaopeng Lan,[a] Chunlei Liu,[a] Xiaodong Yan,[c] Xuewei Fu,[d] Yaochun Liu,[e] Yuan Liu,*[ae] Dapeng Cao,[f] Jingjie Dai,[g] Xiaofen Hong[h] and Chunzhao Liu*[a]

A breakthrough in enhancing visible-light photocatalysis of wide-bandgap semiconductors such as prototypical titania (TiO_2) *via* cocatalyst decoration is still challenged by insufficient heterojunctions and inevitable interfacial transport issues. Herein, we report a novel TiO_2-based composite material composed of *in situ* generated polymorphic nanodomains including carbon nitride (C_3N_4) and (001)/(101)-faceted anatase nanocrystals. The introduction of ultrafine C_3N_4 results in the generation of many oxygen vacancies in the TiO_2 lattice, and simultaneously induces the exposure and growth of anatase TiO_2(001) facets with high surface energy. The photocatalytic performance of C_3N_4-induced TiO_2 for degradation of 2,4-dichlorophenol under visible-light irradiation was tested, its apparent rate being up to 1.49×10^{-2} min^{-1}, almost 3.8 times as high as that for the pure TiO_2 nanofibers. More significantly, even under low operation temperature and after a long-term photocatalytic process, the composite still exhibits exceptional degradation efficiency and stability. The normalized degradation efficiency and effective lifespan of the composite photocatalyst are far superior to other reported modified photocatalysts.

Received 6th February 2022
Accepted 18th March 2022

DOI: 10.1039/d2ra00782g

rsc.li/rsc-advances

1. Introduction

Design of suitable photocatalytic semiconductors is regarded as one of the most promising solutions to effectively utilize the sustainable solar energy to tackle the challenges of energy exhaustion and environmental destruction.[1–3] Titania (TiO_2) has been proved as the most versatile photocatalyst among semiconductors owing to its cost-effectiveness and high stability,.[4] However, TiO_2 as a photocatalyst suffers from large band gap (>3 eV) and a lack of suitable electronic/surface structures, resulting in limited visible-light (400–700 nm) absorption ability and charge carrier separation efficiency.[5–7] Developing high-performance TiO_2 photocatalysts with visible-light response is needed in order to fully utilize and convert the visible solar light.

To overcome these bottlenecks, many strategies have been adopted to strengthen visible light absorption and realize effective conversion. The strategies involve doping/co-doping transition metal ions (*e.g.* copper, vanadium, and iron, *etc.*)[8–10] and/or electronegative anions (*e.g.* boron, carbon, and nitrogen, *etc.*) as well as introducing oxygen/nitrogen vacancies[11–14] into the lattice of photocatalysts. These approaches effectively narrow the original band gap *via* forming impurity energy levels or elevating the original valence band of oxygen.[15,16] However, these dopants thermodynamically and easily agglomerate and locate at the surface/interface layers: a low density of localized states is introduced into the TiO_2 bandgap, resulting in unsatisfactory visible-light absorption and conversion.[13] In addition to the above strategies, optimization of high-surface-energy defects and facets of TiO_2 such as anatase TiO_2(001) represents an effective way for enhancing the photocatalytic activity and efficiency.[17–19] Compared with the dominant and thermodynamically stable TiO_2(101) facet, the TiO_2(001) facet exhibits a high density of unsaturated titanium atoms and surface oxygen atoms for enhanced photocatalytic activity.[20–22] However, according to the Wulff construction and surface energy, only 6% (001) facets can be exposed in the stable anatase TiO_2.[23] More

[a]*State Key Laboratory of Bio-fibers and Eco-textiles, Institute of Biochemical Engineering, The Affiliated Qingdao Central Hospital of Qingdao University, College of Materials Science and Engineering, Qingdao University, Qingdao 266071, China. E-mail: liuyuan@qdu.edu.cn; czliu@qdu.edu.cn*

[b]*Energy Materials and Surface Sciences Unit (EMSSU), Okinawa Institute of Science and Technology Graduate University (OIST), 1919-1 Tancha Kunigami-gun, Onna-son, Okinawa 904-0495, Japan. E-mail: chenfeng.ding@oist.jp*

[c]*Key Laboratory of Synthetic and Biological Colloids, Ministry of Education, School of Chemical and Material Engineering, Jiangnan University, Wuxi 214122, China*

[d]*College of Polymer Science and Engineering, State Key Laboratory of Polymer Materials Engineering, Sichuan University, Chengdu 610065, Sichuan, China*

[e]*Foshan (Southern China) Institute for New Materials, Foshan 528200, China*

[f]*Beijing Advanced Innovation Center for Soft Matter Science and Engineering, Beijing University of Chemical Technology, Beijing 100029, China*

[g]*School of Mechanical and Electronic Engineering, Qingdao Binhai University, Qingdao 266555, Shandong, China*

[h]*Zhejiang Rich Environmental Protection Technology Co., Ltd, Hangzhou 310000, China*

† Electronic supplementary information (ESI) available. See DOI: 10.1039/d2ra00782g

‡ These authors contributed equally.

significantly, these methods have limited accommodation of adsorption of low-energy protons and restraint on recombination of electron and holes, leading to the poor visible light photocatalytic performance. Thus, there is a long-sought-after demand for further improving both the absorption and conversion of visible light for TiO_2 photocatalysts.

To design advanced photocatalysts should integrate three elements, that is, good photochemical properties, high photocatalytic activity, and excellent long-term stability/capacity.[24,25] Designing composite photocatalysts with heterogeneous junctions is an effective approach for tuning the electronic and interface structure,[26,27] that are beneficial for the fast charge transfer.[28,29] Thus far, manifold heterogenous components such as noble metal,[30,31] transition metal oxide/sulfide,[32,33] and metal–organic framework materials,[34,35] *etc.* have been intensively studied and demonstrated to show satisfactory improvement of visible light absorption and photochemical activity. As the most promising alternative photocatalyst to metal-based ones, carbon nitride (C_3N_4) possesses suitable valence energy and conduction band, good chemical/thermal stability, and visible-light harvesting capability.[36–38] After C_3N_4-decoration, the TiO_2-based composites exhibit visible-light absorption and enhanced photocatalytic activity.[39,40] However, the insufficient heterojunctions and inherent poor interfacial compatibility between C_3N_4 and TiO_2 matrix inevitably lead to energy loss during the light transportation and inhibition of charge migration. Therefore, to overcome these issues, more critical efforts on TiO_2-based photocatalysts that can simultaneously realize visible-light harvesting, high photocatalytic activity, and good long-term life span as well as stability are highly needed.

Nanodomains is a nanometer-sized protein found in a natural cell membrane.[41] Constructing suitable biomimetic nanodomains can realize the rapid transportation of ions/electrons in composite media.[42,43] Similarly, we report a polymorphic TiO_2-based composite material formed by *in situ* diverse nanodomains including C_3N_4 and (001)/(101)-faceted anatase nanocrystals. The unique composite structure is fabricated by calcinating the nanofibrous composite precursor of thiourea and tetrabutyl titanate in the air. Induced by *in situ* formation of heterogeneous ultrafine C_3N_4 crystals, oxygen vacancy occurs in the lattice structure and high-surface-energy anatase TiO_2(001) facets are exposed. The resulting composite simultaneously presents excellent photocatalytic activity and a relatively narrow bandgap. As a result, the composite exhibits excellent degradation efficiency of 2,4-dichlorophenol (2,4-DCP) and various organic dyes under visible light with high kinetic rates. Additionally, even under low operation temperature or after a long-term photocatalytic process, the composite still exhibits desirable degradation efficiency and stability.

2. Experimental section

2.1 Materials and chemicals

Tetrabutyl titanate ($C_{16}H_{36}O_4Ti$, CP) was provided by Sinopharm Chemical Reagent Co., China. The sodium hydroxide (KOH, AR), polyvinylpyrrolidone (PVP, $M_w = 1\ 300\ 000$, AR), and thiourea (CN_2H_4S, AR), silver nitrate ($AgNO_3$, AR), benzoquinone (BQ, AR), tertiary butanol (TBA, AR), and ethylene diamine tetraacetic acid (EDTA, AR) were purchased from Aladdin Chemical Co., China. Tertiary butanol (TBA). *N*,*N*-dimethylformamide (DMF, AR) and hydrochloric acid (HCl, AR) were purchased from Sinopharm Chemical Reagent Co. (Shanghai), China. 2,4-DCP was purchased from Macklin Co., China. CR and methylene blue (MB) were bought from the National Pharmaceutical Co., China. Rhodamine-b (Rh-b) was obtained from Tianjin Tianxin Chemical Co., China. All chemicals were used without further purification.

2.2 Preparation of C_3N_4-induced TiO_2 nanofibers and counterparts

As shown in Scheme 1, the TiO_2-based composite nanofibers were prepared by an electrospinning technology and subsequent thermal treatment. The detailed synthesized method is as follows. First, 1 g of PVP was dissolved in anhydrous ethanol (4.5 mL) and N–N dimethylformamide (4.5 mL) to achieve a homogeneous solution. Then thiourea were added into the mixture solvent with various mass (0.1, 0.5, and 1 g), separately. Then 6 mmol tetrabutyl titanate was gradually added into the pre-solution. After full homogenization, the mixture was used as the electrospinning solution. During the electrospinning process, the precursor solution was loaded into a 20 mL plastic syringe pump and injected through a stainless-steel needle with a flow rate of 1 mL h^{-1}. A high positive charge of 16 kV was applied between the needle tip and the collector. The receiving speed of the collector is around 400 rpm. Then, the fibrous membranes were dried at 60 °C in a vacuum oven for 12 hours and calcined in air at 500 °C with an increasing rate of 3 °C min^{-1}. The fibrous membranes were maintained at 500 °C for 2 h to obtain C_3N_4-induced TiO_2 nanofibers. TiO_2 nanofibers were prepared by the same procedures above, except that thiourea was not added in the prepared electrospinning solution.

Similarly, the obtained precursor nanofibers were mixed with ethanol solution of thiourea with a mass ratio of 1 : 1. Then composite was dried at 60 °C in a vacuum oven for 12 hours and calcined in air at the temperature of 500 °C with an increasing rate of 3 °C min^{-1} and maintain at 500 °C for 2 h. The obtained sample is denoted as the C_3N_4/TiO_2.

2.3 Surface and structure characterization

An ultra-micro balance (Mettler Toledo) with an accuracy of 10 μg was used to weigh the samples and chemicals. The microscopic architecture and chemical structure of samples were characterized by SEM (FE-SEM, Supra55, Carl Zeiss) with energy dispersive

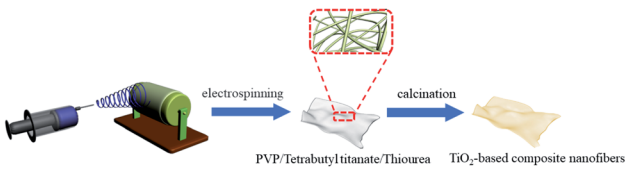

Scheme 1 Flowchart for the synthesis of TiO_2-based composite nanofibers.

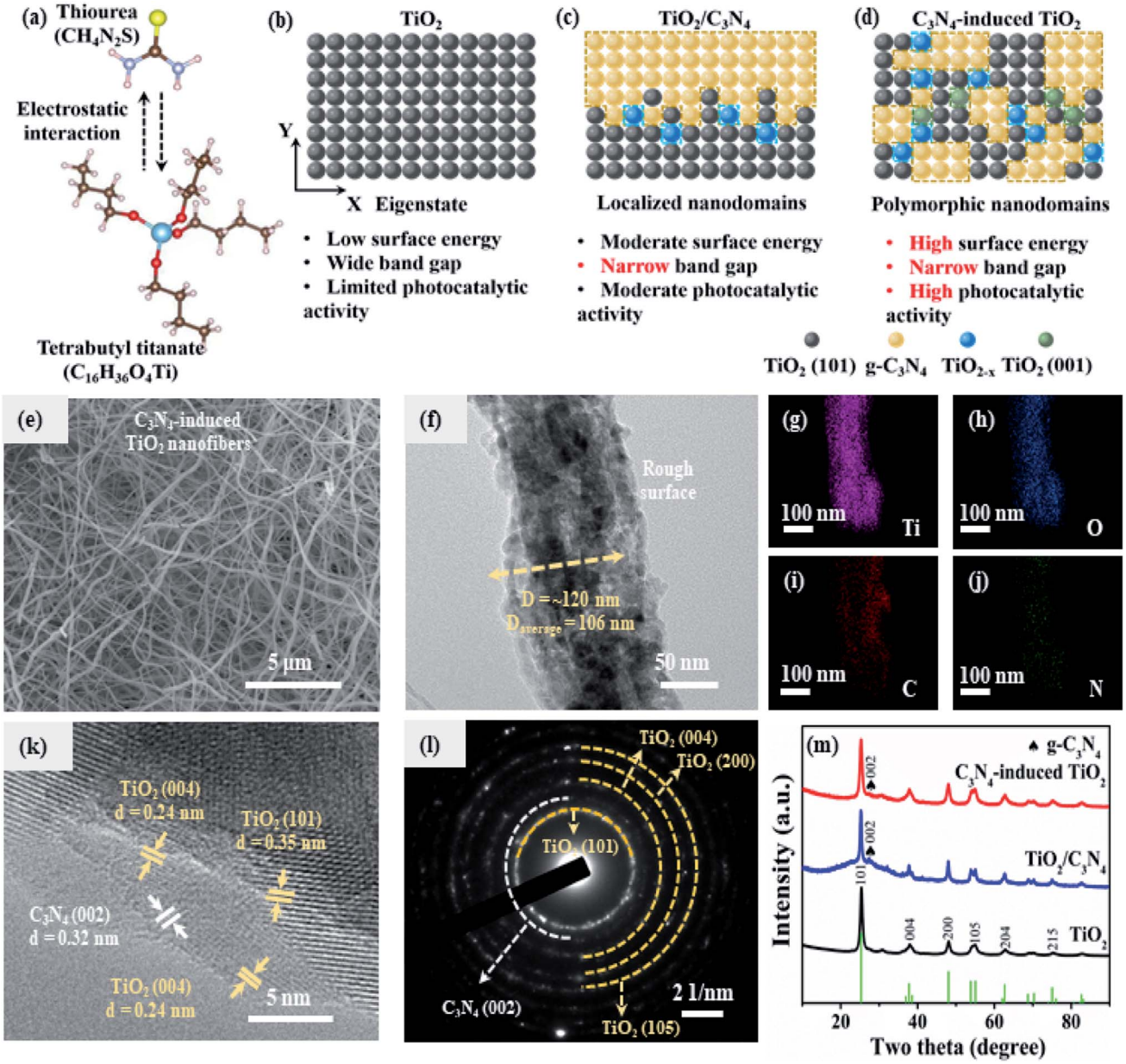

Fig. 1 Schematic illustration and morphologies of C_3N_4-induced TiO_2: (a) schematic illustration of the electrostatic interaction between thiourea and tetrabutyl titanate. (b)–(d) Comparison of constituent and contribution of TiO_2, C_3N_4/TiO_2, and C_3N_4-induced TiO_2. (e) Scanning electron microscope (SEM) of C_3N_4-induced TiO_2 nanofibers. (f) Transmission electron microscope (TEM) images of single nanofiber. (g)–(j) Energy dispersive spectrometer (EDS) elemental mappings of partial C_3N_4-induced TiO_2 nanofiber. (k) High-resolution TEM image of constituents in C_3N_4-induced TiO_2, and (l) selected area electron diffraction. (m) X-ray diffraction spectra of C_3N_4-induced TiO_2 as compared with counterparts.

X-ray (EDX) spectroscopy, a high-resolution transmission electron microscope (HR-TEM, JEM-3010, JEOL), UV-visible spectrophotometer (UV-2700, Shimadzu), Raman spectroscopy (Ar laser, wavelength: 532 nm, RM2000, Renishaw), XPS (ThermoFisher scientific), and a D8 Advance Diffractometer (Bruker) with a Cu Kα source. Nitrogen adsorption/desorption isotherms were collected at 77 K on a Micromeritics ASAP 2020 instrument. The specific surface area was obtained by the Brunauer–Emmett–Teller (BET) method. The pore size distribution was obtained from the density functional theory (DFT) method. The wetting behaviors were characterized by a contact angle analyzer (SL-200KB, KINO). The tap densities of the powders were measured as follows. A certain quantity of powders was added to a dry quartz tube and was then vacuumed until the volume of the powders did not change to measure the volume of the tapped powders. Then the mass and the measured volume of the tapped powders were used to calculate the tap density.

2.4 Evaluation on photocatalytic activity

The photocatalytic activity of the samples was evaluated *via* the photocatalytic degradation of Rh-b and other pollutants under

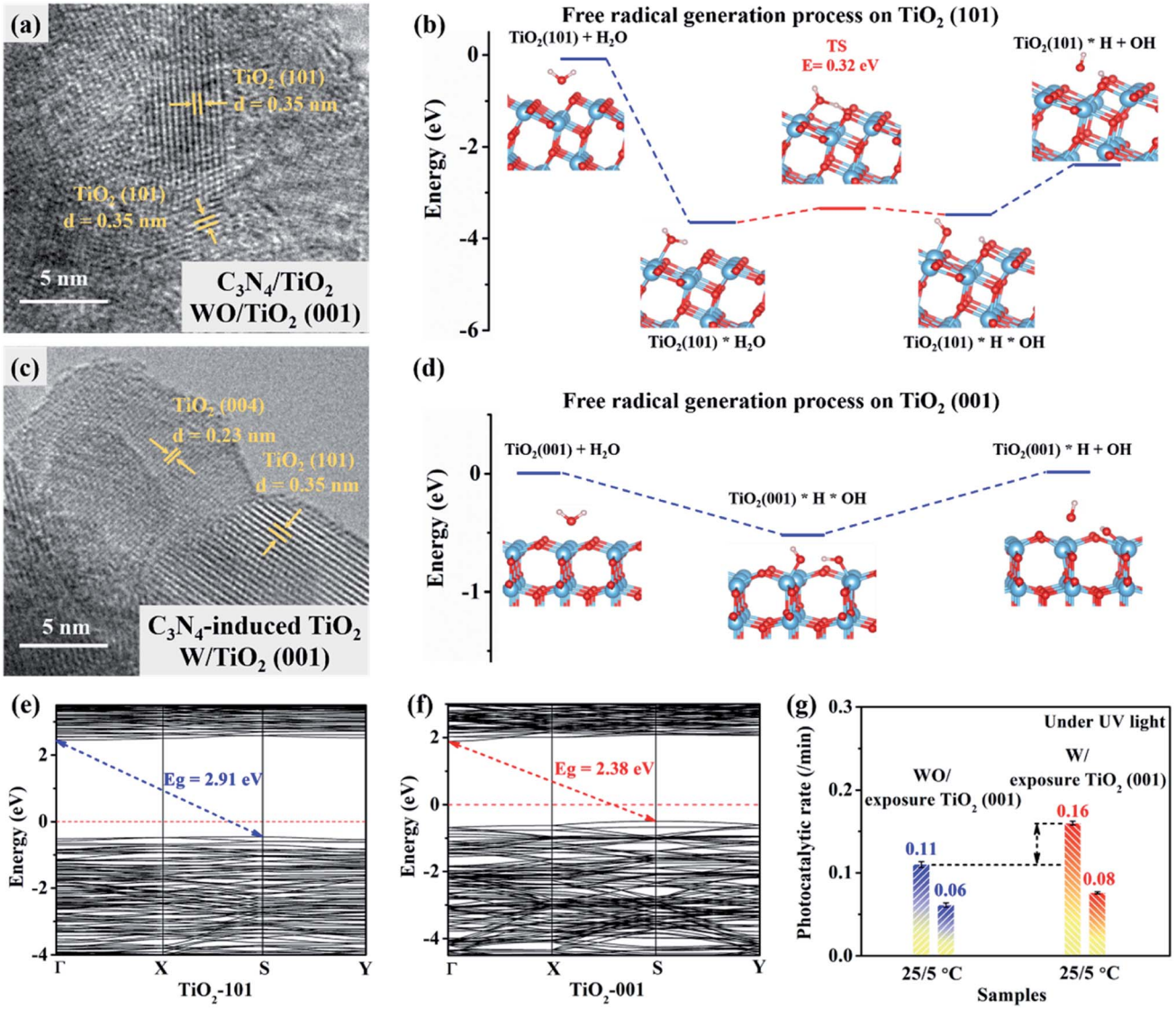

Fig. 2 Photocatalytic activity of samples with/without TiO_2(001) plane: HR-TEM images of each plane in (a) C_3N_4/TiO_2 and (c) C_3N_4-induced TiO_2. Simulated free radical generation process on (b) TiO_2(101) plane and (d) TiO_2(001) plane. Calculated band structures of (e) TiO_2(101) and (f) TiO_2(001) plane. (g) Comparative photocatalytic rates between C_3N_4/TiO_2 and C_3N_4-induced TiO_2 under the UV light.

UV/visible-light irradiation. These experiments were conducted in a photocatalytic reactor. The light source was a 230 W xenon lamp with a UV-light filter from 300 to 400 nm and a visible-light filter from 420 to 780 nm, respectively. 50 mg of the photocatalytic material was added to a 50 mL pollutants reaction mixture (10 mg L^{-1}), including Rh-b, 2,4-DCP, CR, and MB, in a quartz tube. The pH values were controlled by the addition of sodium hydroxide and hydrochloric acid. For 2,4-DCP degradation, the photocatalyst powder and 2,4-DCP solution were mixed in a photochemical glass reactor under magnetic stirring at the room temperature and standard pressure. Prior to irradiation, the reactive system was stirred magnetically in dark for 30 min to reach the adsorption–desorption equilibrium. During the photoreaction process, 3 mL of the solution was collected every 30 min and then centrifuged for 5 min with a rate of 5000 rpm to remove the material. The concentration variation of 2,4-DCP under the UV light was determined by High-performance liquid chromatography (HPLC, Agilent 1260). Before determination, the samples were filtered by 0.22 μm membrane, and then the filtrates were performed using HPLC with the UV detector at 290 nm. The HPLC was equipped with a Kromasil C18 column and worked at 25 °C. The mobile phase was 85 : 15 (v/v) methanol (CH_3OH) and ultrapure water, and the flow rate was 1 mL min^{-1}. The compounds were identified by comparing retention times with standard samples and then quantified with calibration curve method. In addition, for the photocatalytic degradation of Rh-b, CR, and MB, 3 mL of aliquots were collected and sampled at certain time interval of 10 min for subsequent analysis after centrifugation and filtration to remove the photocatalyst. The real time concentrations of dye were determined on UV-visible spectrophotometer at $\lambda =$ 555 nm, $\lambda =$ 497 nm and $\lambda =$ 664 nm for Rh-b, CR and MB,

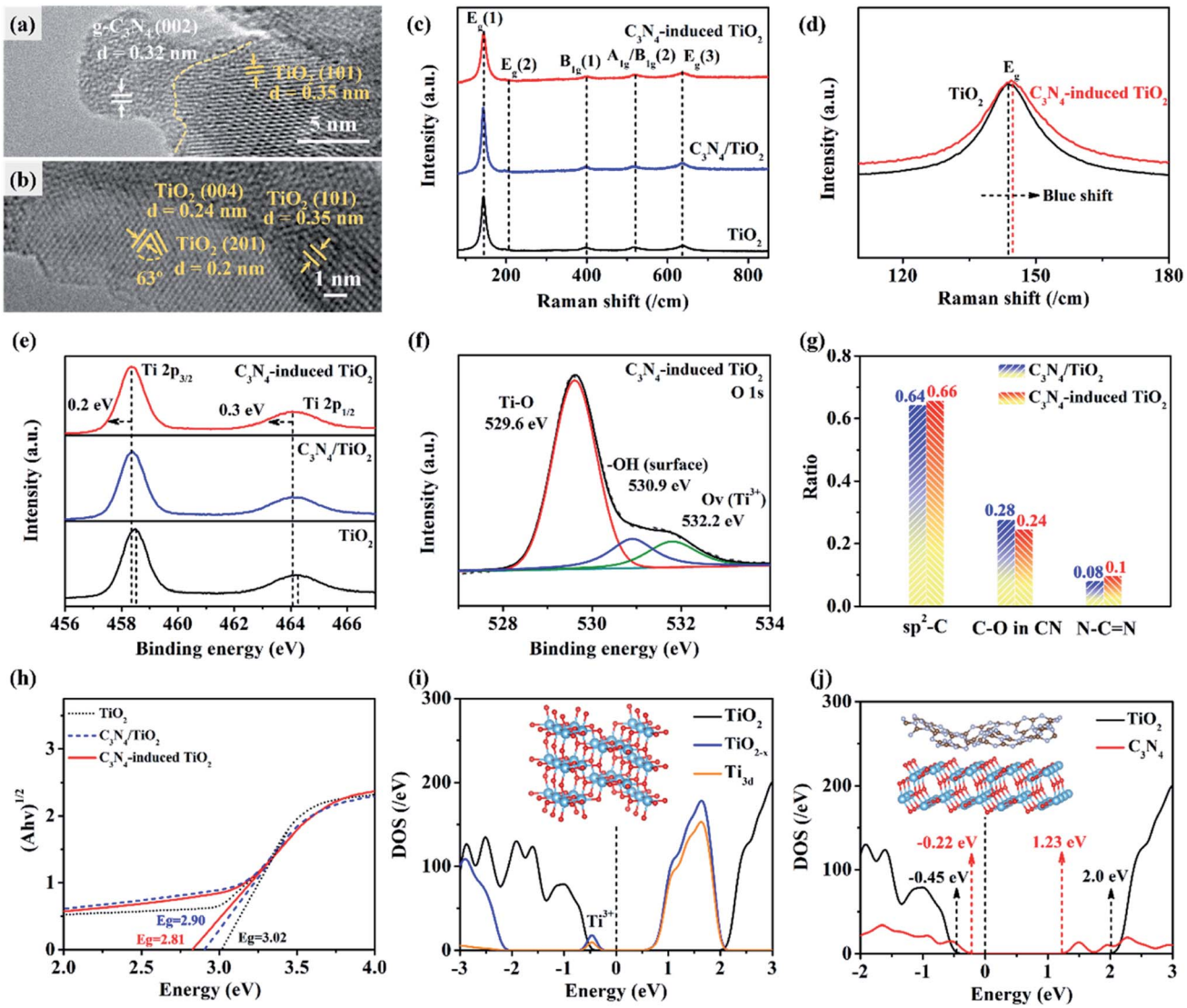

Fig. 3 Characterization on constituent and band gap of C_3N_4-induced TiO_2 as compared with counterparts: (a) and (b) are HR-TEM images of each interface in C_3N_4-induced TiO_2. (c) Raman spectra of C_3N_4-induced TiO_2, C_3N_4/TiO_2, and TiO_2. (d) Magnified partial spectra of C_3N_4-induced TiO_2 and TiO_2. (e) XPS spectra of C_3N_4-induced TiO_2, C_3N_4/TiO_2, and TiO_2. (f) XPS spectra of O 1s in C_3N_4-induced TiO_2. (g) Comparative carbonaceous constituents of C_3N_4/TiO_2 and C_3N_4-induced TiO_2. (h) Kubelka–Munk-transformed reflectance of TiO_2, C_3N_4/TiO_2, and C_3N_4-induced TiO_2. (i) Calculated density of states (DOS) of pure TiO_2 and TiO_{2-x} in C_3N_4-induced TiO_2. (j) Calculated DOS of TiO_2 and C_3N_4 in C_3N_4/TiO_2 and C_3N_4-induced TiO_2.

respectively. Usually, it is ascertained that the removal of pollutants by photocatalysis is related to several reactive oxygen species (ROS) including hydroxyl radical ($^{\bullet}OH$), superoxide radical ($^{\bullet}O^{2-}$) and so on. In order to verify the dominated ROS of 2,4-DCP or Rh-b degradation, the radicals trapping experiments were conducted with the addition of different scavenger agents. EDTA, $AgNO_3$, TBA, and benzo-quinone (BQ) were adopted to quench photo-generated hole (h^+), photo-generated electron (e^-), OH^-, and O^{2-}, respectively. Typically, C_3N_4-induced TiO_2 is added into the 2,4-DCP mixture and stirred for 0.5 h in the dark. After that, the scavengers (5 mM) are added into the liquor and irradiated under visible light for 3 h with continuous stirring.

The first-order kinetic equation during photocatalytic degradation is shown as follows:

$$\ln(C/C_0) = -K_a \times t \quad (1)$$

where K_a is the apparent rate constant, C_0 is the initial concentration, t is reaction time, and C is the concentration at the corresponding time.

The normalized photocatalytic rates are calculated using the equation as follows:

$$K_n = m_1 \times \varepsilon/t \times m_2 \quad (2)$$

where K_n is the normalized photocatalytic rate, m_1 is the total mass of reactant, ε is the final degradation efficiency, t is the total reaction time, and m_2 is the total mass of photocatalyst.

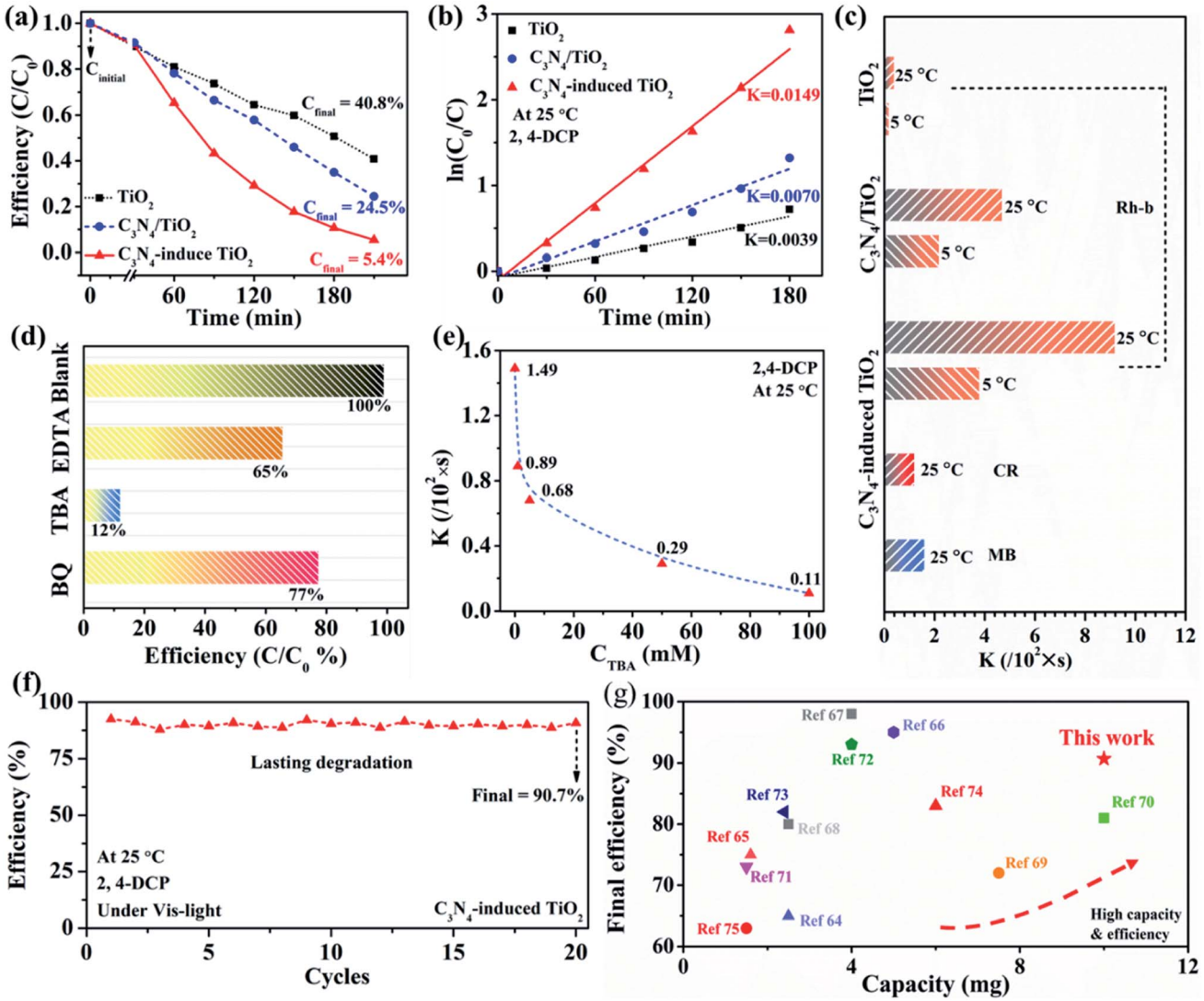

Fig. 4 Photocatalytic activity of C_3N_4-induced TiO_2 under visible light (λ > 420 nm) as compared with counterparts: (a) photocatalytic degradation curve of 2,4-DCP. (b) Pseudo-first-order kinetics curves. (c) Photodegradation kinetic number of Rh-b at various temperatures, CR, and MB. (d) Photocatalytic degradation efficiency with the introduction of EDTA (h^+), TBA ($^{\bullet}OH$), and BQ (O_2^-) as scavengers during the degradation of 2,4-DCP. (e) Kinetic number of C_3N_4-induced TiO_2 with various concentrations of TBA. (f) Long-term photocatalytic degradation of C_3N_4-induced TiO_2. (g) Comparison of final degradation efficiency as a function of maximum degradation capacity between C_3N_4-induced TiO_2 and other reported work.

2.5 Calculation method

The DFT calculations were carried out using the Vienna *Ab initio* Simulation Package (VASP) with the frozen-core all-electron projector-augment-wave (PAW) method. The Perdew–Burke–Ernzerhof (PBE) of generalized gradient approximation (GGA) was adopted to describe the exchange and correlation potential. The cutoff energy for the plane-wave basis set was set to 450 eV. The geometry optimizations were performed until the forces on each ion was reduced below 0.01 eV $Å^{-1}$. The resulting structures were then used to calculate the electronic structures. Here, we adopted DFT + U method for geometry optimization and electronic structure calculation, the effective on-site coulomb interaction parameter of 6 eV was applied to the Ti-3d electrons.

The thiourea and tetrabutyl titanate were placed in a 20 × 20 × 20 $Å^3$ vacuum box to minimize the interactions between neighboring systems, and gamma k-point sampling of the Brillouin zone was used. The adsorption energy, E_{ads}, is calculated using the equation as follows:

$$E_{ads} = E_{thiourea+tetrabutyl\text{-}titanate} - E_{tetrabutyl\text{-}titanate} - E_{thiourea} \quad (3)$$

where $E_{thiourea}$ is the energy of thiourea, $E_{tetrabutyl\text{-}titanate}$ represents the energy of tetrabutyl titanate, and $E_{thiourea+tetrabutyl\text{-}titanate}$ represents the total energy of the adsorbed system.

A vacuum region of 15 Å was added above monolayer TiO_2(101) plane (1 × 3) and tri-layer TiO_2(001) planes (3 × 3) to minimize the interactions between neighboring systems. The climbing image nudged elastic band (CI-NEB) method was

Table 1 Comparing the photocatalytic activity of C_3N_4-induced TiO_2 with selected works in detail

Sample	Light source	Rate constants (min^{-1})	Final efficiency (%)	Capacity (mg)	Ref.
C_3N_4-Induced TiO_2	230 W xenon lamp (420 nm–780 nm)	0.015	90.76	10.86	This work
TiO_2/FeO_X/POM	150 W xenon lamp (>400 nm)	Not available	58	2.03	64
CeO_2/g-C_3N_4	150 W xenon lamp (>420 nm)	Not available	78	1.54	65
$In_2O_3/ZnIn_2S_4$	300 W xenon lamp (>420 nm)	0.0246	95.8	4.75	66
TiO_2/g-C_3N_4	150 W xenon lamp (>400 nm)	0.012	97	3.9	67
Ag_2CrO_4/Ag/g-C_3N_4	500 W xenon lamp (>400 nm)	0.015	80	2.2	68
N-Carbon@ZnO	300 W xenon lamp (380 nm–800 nm)	0.028	72	5.7	69
$SnO_2/Pt/In_2O_3$	500 W xenon lamp (>420 nm)	0.023	80	8.45	70
Ag_3PO_4/Fe_3O_4	250 W LED lamp (>420 nm)	0.056	74	1.34	71
SnO_2/Ag/MoS_2	150 W xenon lamp (>400 nm)	Not available	90	3.89	72
P–g-C3N4	230 W xenon lamp (420 nm–780 nm)	Not available	84	2.1	73
$BiO(OH)_xI_{1-x}$–AgI	150 W xenon lamp (>400 nm)	0.16	85	2.622	74
3S-BN	300 W xenon lamp (380 nm–800 nm)	Not available	63	1.12	75

adopted to calculate free radical (˙OH) generation process on the $TiO_2(101)$ plane. An anatase TiO_2 supercell ($2 \times 2 \times 1$) was used to simulate pure TiO_2, and the model of TiO_{2-X} was built by deleting a O atom in pure anatase TiO_2 supercell. The structure of C_3N_4/TiO_2 composite was built by placing a monolayer C_3N_4 on double-layer $TiO_2(101)$ plane (2×3), and a vacuum region of 15 Å was also added above the C_3N_4/TiO_2 slab model. For geometry optimization, the bottom-layer atoms of $TiO_2(101)$ plane were fixed in their bulk positions.

3. Result and discussion

3.1 Nanoarchitecture of C_3N_4-induced TiO_2

Tuning the interaction and localized homogeneity of molecules in precursors is quite significant for the construction of continuous heterogeneous interfaces in the composite photocatalytic materials.[44] As illustrated in Fig. 1a, there is a strong electrostatic interaction between thiourea and tetrabutyl titanate precursors. Specifically, based on the density factor calculation, the charge density differences between thiourea and tetrabutyl titanate (*e.g.* NH_2–Ti and S–Ti sites) are shown in Fig. S1a and b.† The amino groups on the thiourea exhibit a lower stable distance (~2.83 Å), indicating a stronger interaction with central titanium atom on tetrabutyl titanate than that between C=S and central titanium atoms. In addition, the amino group on thiourea presents an absorption energy of ~1.86 eV (Fig. S1c†), which is much higher than that of C=S (~1.54 eV). In comparison with original TiO_2 (Fig. 1b), C_3N_4/TiO_2 composite (details in ESI†) in Fig. 1c shows a narrow bandgap and enhanced photocatalytic activity due to the introduction of localized heterogeneous nanodomains. Furthermore, *via* regulation of the precursor, C_3N_4-induced TiO_2 (Fig. 1d) displays a narrow bandgap and high photocatalytic activity, which are attributed to the heterogenous junctions and high-surface-energy facets.

Construction of suitable nanostructures with the continuous heterogeneous interface is quite vital for charge separation and migration in composite photocatalytic materials.[25] Specifically, C_3N_4-induced TiO_2 materials exhibit a hierarchical nanofibrous structure (Fig. 1e) with a uniform diameter. As shown in Fig. 1f and S2a,† C_3N_4-induced TiO_2 nanofiber exhibits a grainy surface with an ultrafine diameter of only around 120 nm. The ultrafine nanofibrous structure with the porous surface similar to the schematic illustration in Fig. S2b† is highly beneficial to light transmission, scattering, and absorption.[45] With increasing thiourea in the precursor, nanofibers present curved morphology and smooth surface with an average diameter increasing from 102 to 257 nm (Fig. S3†). Furthermore, the spatial distribution of each element, including Ti, C, O, and N in a single nanofiber, is investigated by energy dispersive spectrometer (EDS) elemental mapping (Fig. 1g–j). As compared with the elemental mapping images of intrinsic Ti and O elements (Fig. 1g and h), the mapping of C and N suggests the uniform distribution of both C and N dopants in the nanofiber. The homogeneous distribution of the substitutional element is highly favorable to the generation of numerous heterogeneous junctions in the nanofibers.[46]

Pore structure and size distribution are crucial structural parameters for spatial mass transfer. The pore structure of C_3N_4-induced TiO_2 is measured using the nitrogen-sorption isothermal analysis with the Barrett–Joyner–Halenda (BJH) model. The C_3N_4-induced TiO_2 nanofibers exhibit a similar specific surface area (22 $m^2\ g^{-1}$) to the counterpart C_3N_4/TiO_2 composite (25 $m^2\ g^{-1}$). However, C_3N_4-induced TiO_2 presents a higher tapping density (~0.11 g cm^{-3}) (Fig. S4†), which is close to that of commercial TiO_2–P25 (~0.13 g cm^{-3}). As shown in Fig. S5a,† the nitrogen adsorption/desorption curves display a type II/IV isotherm curve, which interaction demonstrates the macropore-dominant structure.[47] Furthermore, the pore size distribution of C_3N_4-induced TiO_2 nanofibers is characterized by the density functional theory (DFT) method. The C_3N_4-induced TiO_2 in Fig. S5b† exhibits micropores at around 1.3 nm. The developed microporous structure is highly beneficial to the absorption of small molecules for photocatalysis.

Furthermore, the polymorphic nature of C_3N_4-induced TiO_2 is confirmed by high-resolution transmission electron microscopy (HR-TEM) images (Fig. 1k). The lattice spacing of 0.35 and 0.24 nm are assigned to the stable low-index (101) facet and

high-surface-energy (004) facet of anatase TiO_2, respectively.[48,49] Additionally, the lattice spacing of 0.32 nm is attributed to the (002) plane of C_3N_4.[50] There are some disordered microregions in C_3N_4-induced TiO_2 due to the introduction of N/C heteroatoms and O vacancies. The crystalline composition of C_3N_4-induced TiO_2 can be further investigated by selected area electron diffraction (Fig. 1l). Corresponding diffraction rings of anatase TiO_2 and C_3N_4 can be found, demonstrating the well-crystalline structure. The crystal structures of all the three samples are further confirmed by X-ray diffraction spectra (Fig. 1m). All the three diffraction patterns show six typical and strong diffraction peaks that locate at 25.3°, 37.8°, 48.1°, 53.9°, 62.69° and 75.01°, which are corresponded to the (101), (004), (200), (105), (204) and (215) crystal planes of anatase TiO_2 (JCPDS no. 21-1272), respectively.[51,52] According to the relative (004)/(200) peak intensity ratio of in Fig. S6,† C_3N_4-induced TiO_2 exhibits a higher ratio of ~0.69 than that of TiO_2 (~0.65) and C_3N_4/TiO_2 (~0.67), indicating a better crystal orientation growth along the [001] direction.[53–55] Furthermore, C_3N_4/TiO_2 composite and C_3N_4-induced TiO_2 exhibit additional peaks at around 26.8°, which are assigned to the (002) plane of g-C_3N_4 (JCPDS no. 87-1526) in the composite constituent.[56–58] Besides, as illustrated in Table S1,† according to the Debye–Scherrer formula, C_3N_4-induced TiO_2 exhibits a lower average crystallite size of 9.5 nm in comparison with that of TiO_2 nanofiber and C_3N_4/TiO_2 composite. In a word, well-connected nanosized polymorphic facets of C_3N_4 and anatase TiO_2 are believed to promote the vectorial transfer of photogenerated electrons, thus improving the charge separation and photocatalytic efficiency.[48]

3.2 Catalytic mechanisms and performances of TiO_2(101) and TiO_2(001) plane

It is generally believed that oxidizing radicals in water can oxidize organic pollutants. In order to understand the differences in the photocatalytic process between TiO_2(101) and TiO_2(001) planes, we calculated the free radical (˙OH) generation process by using DFT calculations. Specifically, the C_3N_4/TiO_2 composite in Fig. 2a is dominated by exposed anatase TiO_2(101) with a lattice fringe of 0.35 nm.[48] As shown in Fig. 2b, when H_2O approaches the TiO_2(101) plane, the O atoms in H_2O are adsorbed on 5-coordinated Ti atoms of the TiO_2(101) plane. Then, one of the H atoms in adsorbed H_2O splits to bridge the O atom of the TiO_2(101) plane. The splitting process of H_2O needs to overcome an energy barrier of 0.32 eV. Finally, the free ˙OH is generated after the desorption of adsorbed OH. It is found that ˙OH generation process on the TiO_2(001) plane is much easier than that on the (101) plane. As compared with C_3N_4/TiO_2 in Fig. 2a, C_3N_4-induced TiO_2 in Fig. 2c displays emerging high-energy-surface anatase TiO_2(004) with a lattice fringe of 0.24 nm corresponding to the low-index anatase TiO_2(001) facet.[49] As shown in Fig. 2d, the H_2O on the TiO_2(001) plane is directly split into OH and H. The OH is adsorbed on 5-coordinated Ti atoms, and the H forms a new OH with the bridge O atom of the TiO_2(001) plane. The desorption of OH can generate a free ˙OH. Therefore, the free radical generation process on the TiO_2(001) plane is more energetically favorable than that on the TiO_2(101) plane.

Furthermore, the energy band structures of the TiO_2(101) and TiO_2(001) planes are also calculated in Fig. 2e and f. Energy zero is taken as Fermi level and displayed with a red dashed line. It is found that both TiO_2(101) and TiO_2(001) planes are indirect bandgap semiconductors, and their conduction band minimum (CBM) and valence band maximum (VBM) locate at Γ and S point, respectively. The calculated band gap of TiO_2(001) plane is 2.38 eV, which is 0.53 eV smaller than that of TiO_2(101) plane, indicating higher photocatalytic activity under the same light irradiation. Additionally, the comparison of photocatalytic activity with/without TiO_2(001) facets is further demonstrated by photocatalytic degradation of Rh-b under UV light in Fig. 2g. The C_3N_4-induced TiO_2 with high-surface-energy TiO_2(001) facets exhibits a high kinetic rate of 0.16 min^{-1}, which is higher than that of C_3N_4/TiO_2 (~0.11 min^{-1}). Even at a low operating temperature of 5 °C, C_3N_4-induced TiO_2 still displays a higher photocatalytic activity as compared with C_3N_4/TiO_2 composite. It is further established that the (001) facets of TiO_2 are highly favorable to the enhancement of photocatalytic activity.

3.3 Constituent and electronic structure of C_3N_4-induced TiO_2

The analysis of crystal constituents and structure is quite vital for the investigation of enhancement mechanisms of photocatalytic performance. As shown in Fig. S7a and b,† exposed (101) facets are the most stable and dominant planes in TiO_2 nanofibers. In contrast, the HR-TEM images of C_3N_4-induced TiO_2 indicate the coexistence of various interfaces between C_3N_4 and TiO_2 nanocrystals as well as (101) and (001) facets of anatase TiO_2 (Fig. 3a and b).[50] Raman scattering measurements are employed to characterize the structural properties of C_3N_4-induced TiO_2 (Fig. 3c). The six Raman modes of the anatase phase were detected in both C_3N_4-induced TiO_2 and counterparts, which are assigned to the peaks of 143.6 cm^{-1} ($E_g(1)$), 198.1 cm^{-1} ($E_g(2)$), 398.1 cm^{-1} ($B_{1g}(1)$), 519.5 cm^{-1} ($A_{1g}/B_{1g}(2)$), and 637.5 cm^{-1} ($E_g(3)$).[59,60] As compared with anatase TiO_2, C_3N_4-induced TiO_2 presents a broad $E_g(1)$ at 143.6 cm^{-1} with an obvious blueshift (Fig. 3d). The blueshift and broadening of the E_g peak are attributed to the nano-sized grain (<10 nm) and/or the presence of defects such as (Ti^{3+} and oxygen vacancy).[61]

Furthermore, X-ray photoelectron spectroscopy (XPS) spectra are used to further demonstrate the element constituent in C_3N_4-induced TiO_2. As exhibited in Fig. 3e, the typical peaks of Ti $2p_{3/2}$ and Ti $2p_{1/2}$ in pure TiO_2 are located at 458.5 and 464.3 eV, respectively. Among them, Ti $2p_{3/2}$ peak is used to demonstrate Ti element with different valence states by change of the binding energy. Interestingly, with the introduction of C_3N_4 into TiO_2, both C_3N_4/TiO_2 and C_3N_4-induced TiO_2 exhibit the shift of the total binding energy of Ti element to the low-energy direction, indicating the existence of Ti^{3+}. The increasing Ti^{3+} is attributed to the electron transfer in the coordination environment of O and Ti atoms due to the incorporation of trace amounts of carbon and nitrogen.[62] Additionally, despite similar Ti–O (529.6 eV) and –OH (530.9 eV) peaks to

C_3N_4/TiO_2 (Fig. S8†), C_3N_4-induced TiO_2 shows additional oxygen vacancy (O_v) at 532.2 eV, which is consistent with the previous result in Fig. 3d. The carbonaceous constituents in C_3N_4-induced TiO_2 and its counterpart are further illustrated in Fig. 3f. Notably, based on the fitted carbon curves in Fig. S9,† C_3N_4-induced TiO_2 shows a higher ratio of sp^2-C with lower oxygen content than that of C_3N_4/TiO_2 (Fig. 3g), which is favorable for the electronic conduction and transfer in polymorphic structure.[63] Moreover, more nitrogen-containing functional groups are found in the carbonaceous structure of C_3N_4-induced TiO_2, which is beneficial to amelioration of surface polarity. Accordingly, as shown in Fig. S10,† C_3N_4-induced TiO_2 presents the improved water permeability with a two times lower contacting angle than that of pure TiO_2. The good water wettability and permeability promote the mass transfer between C_3N_4-induced TiO_2 and H_2O as well as targeted molecules, thus improving the photocatalytic efficiency.

Additionally, according to the transformed Kubelka–Munk-transformed reflectance in Fig. 3h, C_3N_4-induced TiO_2 presents a lower bandgap of 2.81 eV than that of TiO_2 nanofibers (~3.02 eV) and C_3N_4/TiO_2 composite (~2.90 eV), respectively. Among that, the bandgap of TiO_2 nanofibers in the study is lower than the theoretical one (~3.2 eV) due to the presence of amorphous constituents and incorporation of trace carbon derived from precursor during calculation. To further reveal the mechanism for reduction of bandgap, the theoretical simulation and calculation in terms of DFT are operated based on previous observed crystal constituents and structure. Specifically, DFT calculated DOS of pure TiO_2 and O-deficient TiO_2 (TiO_{2-x}) is shown in Fig. 3i, in which the energy zero is denoted as Fermi level with a black dashed line. It is found that the Fermi level of pure TiO_2 locates above the VBM, indicating intrinsic semiconductive property. In contrast, for TiO_{2-x}, the Fermi level locates below the CBM, demonstrating n-type semiconductive characteristics.

However, there is an appearance of defect state below the CBM of TiO_{2-x}, which mainly consists of the Ti-3d orbital. The defect state is mainly caused by the reduction of Ti^{4+} to Ti^{3+} in O-deficient TiO_2. The defect state induced by O-vacancy can improve the visible-light absorption of TiO_{2-x} to some extent. However, these defects often act as recombination centers of photogenerated electron–hole pairs, which limits the further improvement of photocatalytic performance of TiO_{2-x} due to the relatively high recombination rate. Moreover, as displayed in Fig. 3j, the Fermi level (energy zero) of C_3N_4 and TiO_2 locate at 0.22 eV and 0.45 eV above each VBM value. Benefiting from the unique combination of Fermi level, the C_3N_4/TiO_2 composite presents a bandgap of 1.45 eV as an intrinsic semiconductor, demonstrating the high potential for visible-light absorption and conversion.

3.4 Photocatalytic performances of C_3N_4-induced TiO_2

The excitation processes of C_3N_4-induced TiO_2 and counterparts under visible light are demonstrated by the photocatalytic oxidation of 2,4-DCP and other various organic dyes. According to the standard plots in Fig. S11,† the concentration of 2,4-DCP as a function of illumination intensity is plotted in Fig. 4a. C_3N_4-induced TiO_2 displays a degradation efficiency of 94.6%, which is much higher than that of TiO_2 (~59.2%) and C_3N_4/TiO_2 (75.5%). Simultaneously, the corresponding plots are in accordance with the first-order kinetic eqn (1). It is found that C_3N_4-induced TiO_2 presents a K_a of 0.015 min^{-1} that is up to two times higher than that of TiO_2 and C_3N_4/TiO_2 (Fig. 4b), demonstrating the enhanced photocatalytic efficiency at room temperature. Furthermore, the photocatalytic activity of C_3N_4-induced TiO_2 is further demonstrated by the photodegradation of different organic dyes. According to standard plots of Rh-b in Fig. S12,† corresponding photodegradation curve and K_a at different operation temperatures are calculated and summarized in Fig. 4c. As compared with TiO_2 and C_3N_4/TiO_2, C_3N_4-induced TiO_2 exhibits a higher photodegradation kinetic rate of 0.092 min^{-1}. As known, low operation temperature has a negative effect on molecular dynamics of the reactant surface, thereby restricts the mass transfer and diffusion process during the photocatalytic reaction. However, even at a low operation temperature (5 °C) in Fig. 4c, C_3N_4-induced TiO_2 still shows a higher K_a of 0.038 min^{-1} based on the degradation process (Fig. S13†) than that of counterparts. As shown in Fig. S14,† the photocatalytic efficiency of C_3N_4-induced TiO_2 decreases with increasing pH value, demonstrating good stability in acidic condition. Additionally, according to the standard plots in Fig. S15† and photocatalytic degradation curve in Fig. S16,† C_3N_4-induced TiO_2 simultaneously displays the good photodegradation ability of CR and MB, which further demonstrates its good universality in degrading various organic dyes.

To explore the main reactive species of C_3N_4-induced TiO_2 during the photodegradation of 2,4-DCP, the trapping experiments were implemented with TBA, EDTA, and BQ as the $^{\bullet}OH$, h^+, and $^{\bullet}O^{2-}$ scavengers, respectively. As shown in Fig. 4d, the initial degradation efficiency of C_3N_4-induced TiO_2 is regarded as 100%. The relative photodegradation efficiency of C_3N_4-induced TiO_2 are generally decreased with introduction of scavengers into the systems, indicating all active species are all participated into the photodegradation process. But with introduction of TBA as $^{\bullet}OH$ scavenger, C_3N_4-induced TiO_2 exhibits a limited photodegradation efficiency of 12%. The sudden drop of photodegradation efficiency demonstrates that the key active specie is $^{\bullet}OH$. With increasing of TBA concentration in Fig. 4e, the K_a of photodegradation process exhibits the nonlinear decreasing relationship, further indicating coexistence of $^{\bullet}OH$ as the key active specie other active species during photodegradation process. As for the degradation of organic dyes such as Rh-b, $^{\bullet}OH$ also plays the major role to degrade the dyes as demonstrated by Fig. S17.† Moreover, the durability and stability of C_3N_4-induced TiO_2 are further investigated by cyclic photocatalytic oxidation reactions of 2,4-DCP. After 20 cycles in Fig. 4f, the photocatalytic efficiency under visible light still retains 90.7%. Simultaneously, C_3N_4-induced TiO_2 maintains an inherent nanofibrous structure with a rough surface (Fig. S18†). In contrast to the reported modified photocatalytic materials (Fig. 4g and Table 1), C_3N_4-induced TiO_2 in this study simultaneously presents a higher degradation capacity and satisfactory final efficiency. The excellent

photocatalytic performances are attributed to stable nanostructure and polymorphic nanodomains/interfaces, which facilitate electron separation and extend the lifetime of the separated electron and hole.

4. Conclusion

In summary, we fabricate a polymorphic TiO_2 composite composed of *in situ* diverse nanodomains including C_3N_4 nanocrystals and (001)-/(101)-faceted anatase. The unique structure is fabricated by calcinating the composite nanofibrous precursor of thiourea and tetrabutyl titanate in air. Induced by *in situ* formation of heterogeneous ultrafine C_3N_4 crystals, more oxygen vacancies can be generated in the TiO_2 lattice structure. And high-surface-energy anatase TiO_2(001) facets are simultaneously exposed. The resulting composite simultaneously presents excellent photocatalytic activity and relatively narrow bandgap. The composite exhibits a degradation efficiency of 94.6% in 2 h under visible light with a high kinetic rate of 0.015 min^{-1}. Additionally, the composite still exhibits excellent durability even under extreme conditions such as low-temperature and acidic environment, and desirable long-term stability with high degradation efficiency. More significantly, the normalized degradation rate and effective durability of the composite photocatalyst are far superior to other reported modified TiO_2 photocatalysts. This work not only leads to a novel TiO_2 composite material, but also provides a new strategy for the design of advanced photochemical semiconductors.

Author contributions

Chunzhao Liu supervised the project. Chenfeng Ding and Yuan Liu conceived the idea, designed the experiments, and participated in the data analysis. Zeju Zhang carried out the fabrication and characterizations. Mang Niu provided support for the DFT stimulation and corresponding analysis. Wei Li, Peitao Xie, Yongxin Li, Xiaodong Yan, Xuewei Fu, Yaochun Liu, Lili Chen, Xiaodong Lan, Chunlei Liu, Jingjie Dai, Xiaofei Hong, and Dapeng Cao provided valuable suggestions for the manuscript. All authors contributed to writing the paper.

Conflicts of interest

There are no conflicts to declare.

Acknowledgements

This work was financially supported by the Natural Science Foundation of Shandong Province (ZR2020QE060), the Key Research and Development Project of Shandong Province (2019GSF109079), the Guangdong Basic and Applied Basic Research Foundation (2019A1515110504, 2020A1515110830), the Medical Science and Technology Development Plan Project of Shandong Province (202104050762), the Qingdao Key Health Discipline Development Fund, the Medical Science and Technology Development Plan Project of Qingdao City (2021-WJZD072, 2021-WJZD069), and the State Key Laboratory of Bio-Fibers and Eco-Textiles (Qingdao University). We also acknowledge the support from the Organizing Committee of the 19th Asian Games in 2022 and Zhejiang province indoor environment depuration industry association.

References

1 S. Chen, T. Takata and K. Domen, *Nat. Rev. Mater.*, 2017, **2**, 1–17.
2 C. Y. Toe, Z. Zheng, H. Wu, J. Scott, R. Amal and Y. H. Ng, *Angew. Chem., Int. Ed.*, 2018, **57**, 13613–13617.
3 Q. Sun, N. Wang, J. Yu and J. C. Yu, *Adv. Mater.*, 2018, **30**, 1804368.
4 X. Chen and S. S. Mao, *Chem. Rev.*, 2007, **107**, 2891–2959.
5 Q. Zhu and D. G. Nocera, *J. Am. Chem. Soc.*, 2020, **142**, 17913–17918.
6 Z. Xing, J. Zhang, J. Cui, J. Yin, T. Zhao, J. Kuang, Z. Xiu, N. Wan and W. Zhou, *Appl. Catal., B*, 2018, **225**, 452–467.
7 T. Wei, Y.-N. Zhu, X. An, L.-M. Liu, X. Cao, H. Liu and J. Qu, *ACS Catal.*, 2019, **9**, 8346–8354.
8 R. Jaiswal, J. Bharambe, N. Patel, A. Dashora, D. Kothari and A. Miotello, *Appl. Catal., B*, 2015, **168**, 333–341.
9 G. Rossi, L. Pasquini, D. Catone, A. Piccioni, N. Patelli, A. Paladini, A. Molinari, S. Caramori, P. O'Keeffe and F. Boscherini, *Appl. Catal., B*, 2018, **237**, 603–612.
10 M. Surówka, M. Kobielusz, M. Trochowski, M. Buchalska, K. Kruczała, P. Broś and W. Macyk, *Appl. Catal., B*, 2019, **247**, 173–181.
11 R. Asahi, T. Morikawa, T. Ohwaki, K. Aoki and Y. Taga, *science*, 2001, **293**, 269–271.
12 J. H. Lee, D. F. Hevia and A. Selloni, *Phys. Rev. Lett.*, 2013, **110**, 016101.
13 T. Wu, P. Niu, Y. Yang, L. C. Yin, J. Tan, H. Zhu, J. T. Irvine, L. Wang, G. Liu and H. M. Cheng, *Adv. Funct. Mater.*, 2019, **29**, 1901943.
14 Y. Lin, C. Yang, S. Wu, X. Li, Y. Chen and W. L. Yang, *Adv. Funct. Mater.*, 2020, **30**, 2002918.
15 N. Nishiyama, Y. Fujiwara, K. Adachi, K. Inumaru and S. Yamazaki, *Appl. Catal., B*, 2015, **176**, 347–353.
16 T. M. Breault and B. M. Bartlett, *J. Phys. Chem. C*, 2012, **116**, 5986–5994.
17 S. Liu, J. Yu and M. Jaroniec, *Chem. Mater.*, 2011, **23**, 4085–4093.
18 G. Liu, H. G. Yang, X. Wang, L. Cheng, J. Pan, G. Q. Lu and H.-M. Cheng, *J. Am. Chem. Soc.*, 2009, **131**, 12868–12869.
19 Y. Gong, X. Quan, H. Yu and S. Chen, *Appl. Catal., B*, 2017, **219**, 439–449.
20 L. Ye, J. Mao, J. Liu, Z. Jiang, T. Peng and L. Zan, *J. Mater. Chem. A*, 2013, **1**, 10532–10537.
21 J. Yu, L. Qi and M. Jaroniec, *J. Phys. Chem. C*, 2010, **114**, 13118–13125.
22 M.-V. Sofianou, C. Trapalis, V. Psycharis, N. Boukos, T. Vaimakis, J. Yu and W. Wang, *Environ. Sci. Pollut. Res.*, 2012, **19**, 3719–3726.
23 M. Lazzeri, A. Vittadini and A. Selloni, *Phys. Rev. B*, 2001, **63**, 155409.

24 Y. Wei, F. Zhang, J. Hao, Y. Ling, Y. Gong, S. Wang, J. Wei and Z. Yang, *Appl. Catal., B*, 2020, **272**, 119035.
25 Y. Wei, N. Yang, K. Huang, J. Wan, F. You, R. Yu, S. Feng and D. Wang, *Adv. Mater.*, 2020, **32**, 2002556.
26 C.-C. Wang, X. Wang and W. Liu, *Chem. Eng. J.*, 2020, **391**, 123601.
27 S. You, Y. Hu, X. Liu and C. Wei, *Appl. Catal., B*, 2018, **232**, 288–298.
28 Y. Lin, H. Liu, C. Yang, X. Wu, C. Du, L. Jiang and Y. Zhong, *Appl. Catal., B*, 2020, **264**, 118479.
29 Y. Lin, C. Yang, Q. Niu and S. Luo, *Adv. Funct. Mater.*, 2022, **32**, 2108814.
30 W. Zhang, G. Li, H. Liu, J. Chen, S. Ma, M. Wen, J. Kong and T. An, *Appl. Catal., B*, 2020, **272**, 118969.
31 Y. Zou, B. Yang, Y. Liu, Y. Ren, J. Ma, X. Zhou, X. Cheng and Y. Deng, *Adv. Funct. Mater.*, 2018, **28**, 1806214.
32 H. Yan, L. Liu, R. Wang, W. Zhu, X. Ren, L. Luo, X. Zhang, S. Luo, X. Ai and J. Wang, *Chem. Eng. J.*, 2020, **401**, 126052.
33 G. Malekshoar, K. Pal, Q. He, A. Yu and A. K. Ray, *Ind. Eng. Chem. Res.*, 2014, **53**, 18824–18832.
34 J. Qin, J. Wang, J. Yang, Y. Hu, M. Fu and D. Ye, *Appl. Catal., B*, 2020, **267**, 118667.
35 M. Valero-Romero, J. Santaclara, L. Oar-Arteta, L. Van Koppen, D. Osadchii, J. Gascon and F. Kapteijn, *Chem. Eng. J.*, 2019, **360**, 75–88.
36 X. Wang, K. Maeda, A. Thomas, K. Takanabe, G. Xin, J. M. Carlsson, K. Domen and M. Antonietti, *Nat. Mater.*, 2009, **8**, 76–80.
37 C. Huang, Y. Wen, J. Ma, D. Dong, Y. Shen, S. Liu, H. Ma and Y. Zhang, *Nat. Commun.*, 2021, **12**, 1–8.
38 Q. Zhang, Y. Peng, Y. Lin, S. Wu, X. Yu and C. Yang, *Chem. Eng. J.*, 2021, **405**, 126661.
39 Q. Sun, K. Lv, Z. Zhang, M. Li and B. Li, *Appl. Catal., B*, 2015, **164**, 420–427.
40 Y. Wang, W. Yang, X. Chen, J. Wang and Y. Zhu, *Appl. Catal., B*, 2018, **220**, 337–347.
41 J. F. McKenna, D. Rolfe, S. E. Webb, A. F. Tolmie, S. W. Botchway, M. L. Martin-Fernandez, C. Hawes and J. Runions, *Proc. Natl. Acad. Sci.*, 2019, **116**, 12857–12862.
42 P. Maksymovych, A. N. Morozovska, P. Yu, E. A. Eliseev, Y.-H. Chu, R. Ramesh, A. P. Baddorf and S. V. Kalinin, *Nano Lett.*, 2012, **12**, 209–213.
43 W. Wang, Y. Zhang, G. Xu, L. Peng, B. Ding, Y. Wang, Z. Hou, X. Zhang, X. Li and E. Liu, *Adv. Mater.*, 2016, **28**, 6887–6893.
44 H. Zhang, G. Liu, L. Shi and J. Ye, *Adv. Energy Mater.*, 2018, **8**, 1701343.
45 Y. Gao, N. Yan, C. Jiang, C. Xu, S. Yu, P. Liang, X. Zhang, S. Liang and X. Huang, *Appl. Catal., B*, 2020, **268**, 118737.
46 G. Liu, L.-C. Yin, J. Wang, P. Niu, C. Zhen, Y. Xie and H.-M. Cheng, *Energy Environ. Sci.*, 2012, **5**, 9603–9610.
47 Y. Liu, C. Ding, P. Xie, X. Yan, M. Feng, Y. Liu, C. Liu, Y. Yu and Y. Lin, *Mater. Chem. Front.*, 2021, **5**, 3216–3225.
48 Z. Tong, D. Yang, T. Xiao, Y. Tian and Z. Jiang, *Chem. Eng. J.*, 2015, **260**, 117–125.
49 L. Gu, J. Wang, Z. Zou and X. Han, *J. Hazard. Mater.*, 2014, **268**, 216–223.
50 Y. Tan, Z. Shu, J. Zhou, T. Li, W. Wang and Z. Zhao, *Appl. Catal., B*, 2018, **230**, 260–268.
51 X. He, M. Wu, Z. Ao, B. Lai, Y. Zhou, T. An and S. Wang, *J. Hazard. Mater.*, 2021, **403**, 124048.
52 E. Kusiak-Nejman, A. Wanag, J. Kapica-Kozar, Ł. Kowalczyk, M. Zgrzebnicki, B. Tryba, J. Przepiórski and A. W. Morawski, *Catal. Today*, 2020, **357**, 630–637.
53 M. Liu, L. Piao, W. Lu, S. Ju, L. Zhao, C. Zhou, H. Li and W. Wang, *Nanoscale*, 2010, **2**, 1115–1117.
54 H. G. Yang, C. H. Sun, S. Z. Qiao, J. Zou, G. Liu, S. C. Smith, H. M. Cheng and G. Q. Lu, *Nature*, 2008, **453**, 638–641.
55 F. Tian, Y. Zhang, J. Zhang and C. Pan, *J. Phys. Chem. C*, 2012, **116**, 7515–7519.
56 L. Ge, *Mater. Lett.*, 2011, **65**, 2652–2654.
57 L. Ye, J. Liu, Z. Jiang, T. Peng and L. Zan, *Appl. Catal., B*, 2013, **142**, 1–7.
58 M. Zhang, N. Han, Y. Fei, J. Liu, L. Xing, A. Núñez-Delgado, M. Jiang and S. Liu, *J. Environ. Manage.*, 2021, **297**, 113311.
59 J. A. Rengifo-Herrera, M. Blanco, J. Wist, P. Florian and L. R. Pizzio, *Appl. Catal., B*, 2016, **189**, 99–109.
60 Y. Liu, C. Ding, X. Yan, P. Xie, B. Xu, L. Chen, Y. Liu, C. Liu, Y. Yu and Y. Lin, *Chem. Eng. J.*, 2021, **420**, 129894.
61 A. Naldoni, M. Allieta, S. Santangelo, M. Marelli, F. Fabbri, S. Cappelli, C. L. Bianchi, R. Psaro and V. Dal Santo, *J. Am. Chem. Soc.*, 2012, **134**, 7600–7603.
62 H. Qian, Q. Hou, E. Duan, J. Niu, Y. Nie, C. Bai, X. Bai and M. Ju, *J. Hazard. Mater.*, 2020, **391**, 122246.
63 C. Ding, L. Huang, X. Yan, F. Dunne, S. Hong, J. Lan, Y. Yu, W. H. Zhong and X. Yang, *Adv. Funct. Mater.*, 2020, **30**, 1907486.
64 J. Yu, T. Wang and S. Rtimi, *Appl. Catal., B*, 2019, **254**, 66–75.
65 M. Humayun, Z. Hu, A. Khan, W. Cheng, Y. Yuan, Z. Zheng, Q. Fu and W. Luo, *J. Hazard. Mater.*, 2019, **364**, 635–644.
66 Q. Zhu, Y. Sun, S. Xu, Y. Li, X. Lin and Y. Qin, *J. Hazard. Mater.*, 2020, **382**, 121098.
67 A. Zada, Y. Qu, S. Ali, N. Sun, H. Lu, R. Yan, X. Zhang and L. Jing, *J. Hazard. Mater.*, 2018, **342**, 715–723.
68 C. Feng, Y. Deng, L. Tang, G. Zeng, J. Wang, J. Yu, Y. Liu, B. Peng, H. Feng and J. Wang, *Appl. Catal., B*, 2018, **239**, 525–536.
69 X. Chen, X. Xu, J. Cui, C. Chen, X. Zhu, D. Sun and J. Qian, *J. Hazard. Mater.*, 2020, **392**, 122331.
70 Y. Sun, Q. Zhu, B. Bai, Y. Li and C. He, *Chem. Eng. J.*, 2020, **390**, 124518.
71 K. Talukdar, B.-M. Jun, Y. Yoon, Y. Kim, A. Fayyaz and C. M. Park, *J. Hazard. Mater.*, 2020, **398**, 123025.
72 B. Khan, F. Raziq, M. Bilal Faheem, M. Umar Farooq, S. Hussain, F. Ali, A. Ullah, A. Mavlonov, Y. Zhao, Z. Liu, H. Tian, H. Shen, X. Zu, S. Li, H. Xiao, X. Xiang and L. Qiao, *J. Hazard. Mater.*, 2020, **381**, 120972.
73 J. Ma, K. Wang, C. Wang, X. Chen, W. Zhu, G. Zhu, W. Yao and Y. Zhu, *Appl. Catal., B*, 2020, **276**, 119150.
74 H. Ji, L. Zhang and C. Hu, *Appl. Catal., B*, 2017, **218**, 443–451.
75 C. Feng, L. Tang, Y. Deng, G. Zeng, J. Wang, Y. Liu, Z. Chen, J. Yu and J. Wang, *Appl. Catal., B*, 2019, **256**, 117827.